Pathways for Hydrogen Absorption into Zircaloy-2 under Cathodic Polarization Assessed by Scanning Electrochemical Microscopy, Scanning Electron Microscopy, and Electrochemical Impedance Spectroscopy

Catherine Nowierski, James J. Noël, David W. Shoesmith and Zhifeng Ding

Email alerting service	Receive free email alerts when new articles cite this article - sign up in the box at the top right corner of the article or click here

Pathways for Hydrogen Absorption into Zircaloy-2 under Cathodic Polarization Assessed by Scanning Electrochemical Microscopy, Scanning Electron Microscopy, and Electrochemical Impedance Spectroscopy

Catherine Nowierski, James J. Noël,* David W. Shoesmith,,z and Zhifeng Ding***

Department of Chemistry, The University of Western Ontario, Chemistry Building, London, Ontario N6A 5B7, Canada

Hydrogen absorption by Zircaloy-2 has been studied in neutral sodium sulfate solutions using steady-state polarization measurements, electrochemical impedance spectroscopy (EIS), and scanning electrochemical microscopy (SECM). For applied potentials < -1 V (vs. saturated calomel electrode, SCE), water reduction occurs in faults in the passive oxide covering the alloy. For potentials ≤ -1.3 V_{SCE}, SECM detects a distribution of reactive locations on the electrode surface. Matched SECM and SEM images of the same electrode surface show more reactive sites to be located in the β-phase grain boundaries than on the α-grains. The reactivity of surface locations was determined using SECM probe approach curves. Secondary phase particles incorporating impurities such as Fe, Ni, and Cr as $Zr(Fe, Cr)_2$ and $Zr_2(Fe, Ni)$ are particularly reactive spots, which may act as "windows" for hydrogen absorption into the alloy. This claim is supported by the observation that the surface of the α-grains remains passive even at potentials as low as -2.0 V_{SCE}. The need to include a Warburg impedance element in modeling EIS recorded at potentials ≥ -1.3 V_{SCE} suggests that H_2O reduction is confined to tight flaws in the oxide at grain boundary locations.
© 2012 The Electrochemical Society. [DOI: 10.1149/2.006301jes] All rights reserved.

Materials used in nuclear reactors must withstand severe environmental conditions, including high neutron fluxes, gamma and beta radiation fields, and high temperatures and pressures.[1–3] Zirconium alloys meet these demands and are of great importance as in-core materials in the nuclear industry due to their low neutron capture cross-section. Zircaloy-2 is an example of such a material used for calandria and guide tubes in CANDU (CANada Deuterium Uranium) reactors developed by Atomic Energy of Canada Limited (AECL) in the late 1950s. The alloying elements (Cr, Fe, Ni, Sn) added to produce the Zircaloy-2 alloy influence the material's mechanical properties and corrosion resistance.[4] Due to their low solubility in Zr, Cr, Fe, and Ni segregate to stabilize the β-phase (primarily forming $Zr(Fe, Cr)_2$ and $Zr_2(Fe, Ni)$ intermetallics),[1,5–9] while Sn dissolves in the stable α-phase matrix.[5,10]

Recently, we have been studying the properties of oxides on Ti[11,12] and Zr alloys.[13] Like the more commonly studied Ti alloys, Zr alloys are susceptible to hydrogen absorption, which can lead to embrittlement and, thus, mechanical failure. Intermetallic precipitate particles, especially ones containing Fe, were proposed to be sites through which H could gain access into the metal.[6,14,15] Resolution of the exact mechanism by which this occurs requires the application of techniques able to reveal reactivity on a micrometer scale.

The oxide film on Ti is a wide bandgap semiconductor with a bandgap of 3.05 eV, and slight deviations from stoichiometry (TiO_{2-x}) give the oxide film n-type characteristics.[16] These n-type characteristics can be attributed to a combination of oxygen vacancies and interstitial Ti^{III} ions, which lead to the trapping of electrons in an orbital band just below the conduction band edge.[17,18] When cathodically polarized to potentials below the flatband potential (-0.54 V vs. the saturated calomel reference electrode (SCE)[16]), redox transformations within the passive oxide ($Ti^{IV} \rightarrow Ti^{III}$) lead to the availability of multiple oxidation states and a consequent increase in the conductivity of the film. This facilitates electron transfer across the film/solution interface and allows the reduction of protons, an electrochemical process accompanied by absorption of H into the oxide.[19,20] According to Ohtsuka et al.[21] this coupled redox transformation-hydrogen absorption process can be described by the reaction:

$$ TiO_2 + xH^+ + xe^- \rightarrow TiO_{2-x}(OH)_x \qquad [1] $$
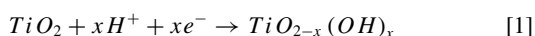
By contrast, ZrO_2 is a good insulator with a large bandgap (5.7 eV),[22] and under cathodic polarization, no similar redox trans-

formation (i.e., $ZrO_2 + xH^+ + xe^- \rightarrow ZrO_{2-x}(OH)_x$) has been observed.[22] The flatband potential for the oxide, -1.26 V_{SCE},[22] is much more negative, which shifts the cathodic current region to lower potentials on ZrO_2 than on TiO_2 films.[23]

Scanning electrochemical microscopy (SECM) is an analytical technique that is widely used to measure qualitative and quantitative chemical reactivities, using an ultramicroelectrode biased with a potential to probe the vicinity of a substrate.[24–26] We have recently employed SECM to demonstrate the increased reactivity of oxide-covered Ti-2 (commercial purity, ASTM Grade-2 titanium)[11] and Ti-7 (ASTM Grade-7 titanium)[12] when the transformation represented by Equation 1 is cathodically-induced. These studies also showed that, on this alloy, when passivated on open circuit, reactive locations were cathodically stimulated at potentials positive to the flatband potential. These locations were shown to coincide with Fe-containing β-phase and intermetallic particles, Ti_xFe, located along the grain boundaries of the α-matrix for Ti-2,[11] and active TiPdFe grain boundary phases for the Pd-containing Ti-7.[12] These investigations[11,12] illustrate that the secondary phases containing the impurity Fe and the alloying element Pd are cathodically activated at less negative potentials than those required to reduce the oxide via the transformation of Equation 1. This raises the question whether these locations can act as "windows" allowing H to be adsorbed into the substrate by bypassing the oxide.[27]

Correlation between SECM and scanning electron microscopy (SEM) images[13] of the same locations on a sample of commercially pure Zr suggested that this material could be cathodically activated at potentials below the flatband potential at surface locations with high impurity Fe contents. The study described in this paper tries to correlate the surface microstructure and reactivity of Zircaloy-2 under cathodic polarization. Like Ti-2, Zircaloy-2 has Fe-containing secondary phase particles (SPPs),[8,14] $Zr(Fe, Cr)_2$ and $Zr_2(Fe, Ni)$. These phases have been shown to support larger cathodic currents than does Zr when under cathodic polarization.[9,28] This suggests that these phases, when present in Zircaloy–2, will act as preferential cathodes. However, Cox et al.[29,30] suggest that H adsorption was not associated with these SPPs, but rather with active cathodic pit sites left behind by the $Zr(Fe, Cr)_2$ SPPs and by cracks and small holes in the oxide.

Herein, for the first time, we image the Zircaloy-2 surface under cathodic polarization, using SECM to determine whether the cathodic sites can be observed. By superimposing SECM images on SEM images of the same area we have been able to correlate localized surface reactivity with the microstructure of the sample. These observations, coupled with electrochemical impedance spectroscopy (EIS) performed over a range of applied potentials, have yielded a better understanding of possible H adsorption routes into Zircaloy-2.

Experimental

Chemicals.— Sodium sulfate (Na_2SO_4, Anhydrous, Caledon Laboratories Ltd., Georgetown, Ontario) was dissolved in deionized water (Milli-Q, Millipore, Bedford, Massachusetts, 18.2 $M\Omega \cdot cm$ resistivity) to produce a 0.1 M supporting electrolyte solution. Ferrocenemethanol, (Fc, 97%, Aldrich, Mississauga, Ontario) at a concentration of 0.9 mM, was added to the above solution to act as the redox mediator necessary for SECM imaging and probe approach curve (PACs) measurements. Purging of solutions with argon was only performed during EIS measurements.

Zircaloy-2 preparation.— Commercial Zircaloy-2 (Zr-1.5Sn-0.14Fe-0.1Cr-0.05Ni-0.01Hf wt%) (obtained from AECL, Chalk River, ON) was ground with SiC paper to a 1200 grit finish, and then polished with Al_2O_3 suspensions to 0.05 μm to produce a mirror finish, allowing a reduction of the effects of surface topography on imaging. The sample was then rinsed in Type-1 water, and placed in a desiccator to dry for 24 h after polishing to ensure that a uniform, native air-formed oxide layer had formed on the surface before experimentation.

SEM.— All SEM images were recorded using an electron microscope (Leo1540 FIB/SEM with CrossBeam, Zeiss Nano Technology Systems Division).

SECM.— Constant height ($\sim$2.5 μm tip-to-substrate distance) SECM experiments were carried out using a custom-built system.[31,32] In brief, positioning was achieved with a FREEDOM 1500-3 Nano Robot system (EXFO Burleigh Products Group, Inc., Canada). The data acquisition systems consisted of a computer with virtual instruments programmed in LabVIEW (Version 7, National Instruments, Austin, TX), a general purpose interface bus (GPIB) board (PCI-GPIB, National Instruments) to communicate with the 8200 controller, and a 16-bit DAQ card (PCI-6052E, National Instruments) with a connection board (BNC-2090, National Instruments). A four electrode electrochemical arrangement incorporating a Pt counter electrode, a reference electrode, a carbon ultramicroelectrode (UME), and the Zircaloy-2 substrate, was used with a bipotentiostat (CHI-832, CH Instruments, Austin, TX) to simultaneously control the potentials of both the UME and the Zircaloy-2 substrate. The reference electrode was Ag/Ag_2SO_4 in 0.1 M Na_2SO_4 (0.683 V_{SHE}), with the potential scale verified by taking the ferrocenemethanol oxidation potential as an internal reference with a potential of 0.436 V_{SHE}.[33] All potential measurements reported here are referred to the SCE scale (0.241 V_{SHE}). The UME, which was prepared according to the procedure described elsewhere,[11] had a 7.0 μm diameter with a glass sheath to carbon fiber radius ratio (RG) value of 3.

SECM images were recorded at room temperature with the UME biased to 0.23 V_{SCE} to maintain the oxidation of the mediator, Fc (to Fc^+), under diffusion control. Potentials between −0.12 V_{SCE} and −1.92 V_{SCE} were applied to the Zircaloy-2 substrate while a 100 × 100 μm (128 × 128 pixel) area of the substrate was imaged by SECM at a scan rate of 10 μm s^{-1}.

Probe approach curves (PACs) were obtained by measuring the current at the UME tip as a function of the tip-to-substrate distance, with the Zircaloy-2 maintained at various applied potentials. The approach rate of the probe tip to the substrate was 1.0 μm s^{-1}. The current was normalized with respect to the limiting tip current when the UME was far away from the substrate. COMSOL multiphysics software (version 3.4, COMSOL, Boston, MA) was used to simulate the PACs, which could be compared to experimental curves to determine electron transfer rate constants (k)[12,13] for the reduction of the Fc^+ at specific locations on the substrate.

Correlation between SECM and SEM images[13] of the same surface locations was realized following the same methodology used for commercial purity Zr.
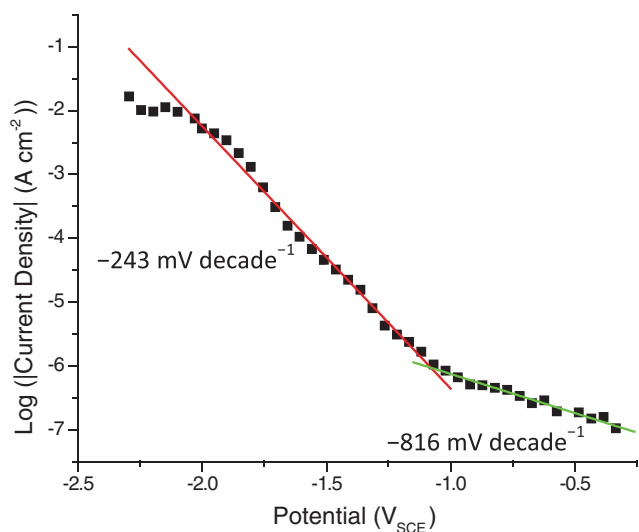
Polarization curves and EIS.— A potentiostat (model 1287, Solartron Analytical, UK) and frequency response analyzer (model 1252, Solartron Analytical) were used to record polarization curves and EIS spectra on 0.78 cm^2 disk-shaped Zr working electrodes in a 1 L electrochemical cell equipped with Pt foil counter electrode and SCE reference. All potential measurements are referred to the SCE scale. Corrware and Corrview software (Scribner Associates, Southern Pines, NC) were used to control experiments and to analyze data. The working electrode potential was held constant at each potential for one hour prior to recording each impedance spectrum. EIS was performed by applying a sinusoidal potential waveform of 10 mV amplitude at specific potentials over the frequency range 10 kHz to 10 mHz. Prior to analysis, EIS data were checked for compliance with four constraints (causality, linearity, stability, and finiteness) by linear Kronig-Kramers transforms using a lab-built code according to the method of Boukamp.[34]

Results and Discussion

Figure 1a shows the microstructure of an unetched Zircaloy-2 specimen. The SEM image was taken using an InLens detector at
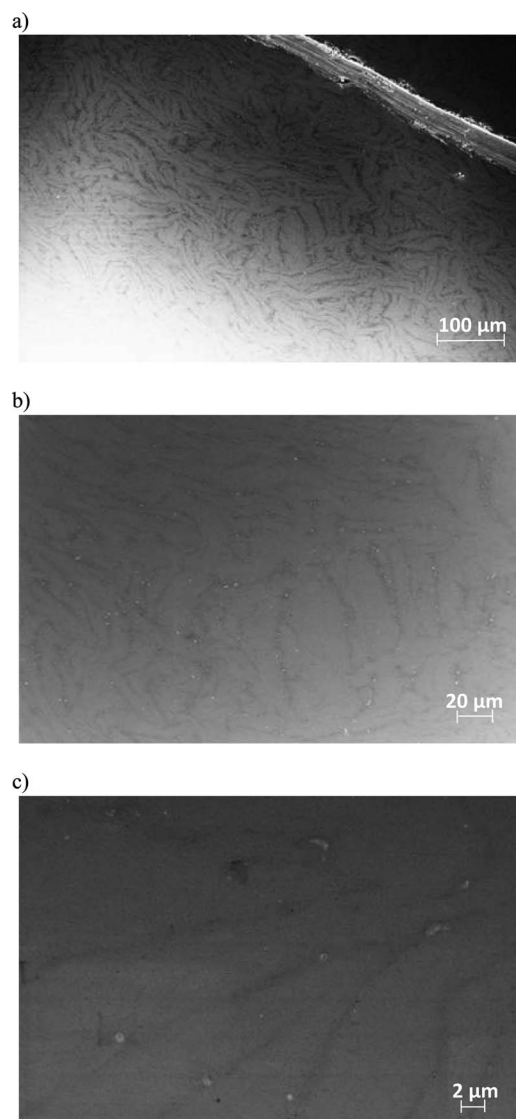

Figure 1. SEM images of a Zircaloy-2 surface showing α- (light) and β-phase (dark) regions, at a series of increasing magnifications, showing secondary phase particles on β-phase grain boundary regions.

Figure 2. Potentiostatic polarization curve for Zircaloy-2 in 0.1 M sodium sulfate solution, with slopes indicated.

5 kV, an open aperture, a high current setting, and a 7 mm working distance, to emphasize the two-phase structure rather than the surface topography. In this image the interwoven α- (light region) and β-phase (dark region) microstructure can be clearly seen. This structure is clearer at higher magnifications, Figure 1b-1c, and the SPPs (bright spots), which decorate the grain boundaries between the Zr α-grains, are clearly visible. These SPPs are between 0.1 and 1 μm in diameter, which is consistent with the published literature.[8]

The potentiostatic polarization curve recorded in 0.1 M Na_2SO_4 is shown in Figure 2. Small H_2O reduction currents began to flow at potentials ≤ -0.33 V_{SCE}, and the cathodic current magnitude became substantial at potentials ≤ -1.3 V_{SCE}. This is consistent with previous observations[13] and within expected values, based on the flatband potential of -1.26 V_{SCE}. The polarization curve displays two linear regions; (1) E ≥ -1.1 V_{SCE} with a Tafel slope of -816 mV/decade, and (2) E < -1.1 V_{SCE} with a Tafel slope of -243 mV/decade. Both of these Tafel slopes are of substantially higher magnitude than the -120 mV/decade expected if the rate of the cathodic reaction,

$$2H_2O + 2e^- \rightarrow H_2 + 2OH^- \qquad [2]$$
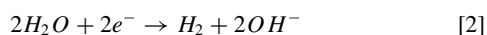
was controlled by the first electron transfer step:

$$H^+ + e^- \rightarrow H_{ads} \qquad [3]$$
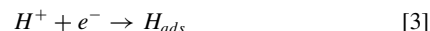
Equation 3 is expected to be rate-controlling on an oxide-covered surface.

No significant variations in current across the Zircaloy-2 surface were detected in SECM images until the Zircaloy-2 substrate was cathodically polarized to a potential of ~ -1.3 V_{SCE}, at which point regions of high (blue) and low (red) current emerged, Figure 3. This is considerably more cathodic than the potential of ~ -1.1 V_{SCE} at which the log I vs E slope changed. The high current regions correspond to reactive sites at which Fc^+, formed at the UME tip, was reduced back to Fc. Further cathodic polarization of the Zircaloy-2 expanded and eventually interlinked these high current regions, Figure 3c. One possibility is that these reactive sites are locations at which complete oxide-coverage was not achieved after 24 hours of air exposure. However, the large Tafel slopes, especially over the potential range of -0.3 V_{SCE} to -0.9 V_{SCE}, clearly indicate oxide coverage at these locations at potentials below those at which these reactive sites were first observed.

Figure 4 shows superimposed SECM images (taken at -1.3 V_{SCE}) and SEM images of the same surface area, revealing that the regions of high (blue) and low (red) current in the SECM image overlap with the β- (dark) and α-phase (light) regions in the SEM image, respectively; i.e., heightened reactivity on the Zircaloy-2 sample occurs at the grain boundary regions between the Zr α-grains. The methodology used to superimpose images was described elsewhere.[13] Murai et al.[28,35] claimed that SPPs containing Fe acted as preferential cathodic sites for H_2O reduction and H absorption since the oxide covering them was more defective than that located on the grains. Under cathodic polarization (to E ≤ -1.3 V_{SCE}) this oxide is more readily reduced, resulting in an increase in the reduction rate of the Fc^+ at these locations, as observed previously for similar precipitates in Ti.[11] By contrast, the reduction rate of Fc^+ is considerably lower on the α-grains, consistent with coverage by a much more defect-free oxide on these locations.

PACs were recorded to quantify changes in reactivity between locations on α- grain surfaces and in grain boundaries as the Zircaloy-2 substrate potential was changed from -0.12 V_{SCE} to -1.92 V_{SCE} in 300 mV sequential increments, Figure 5. These PACs were then matched with PACs simulated using the model, as described elsewhere,[11–13,31] and electron transfer rate constants (k) for the reduction of the Fc^+ on the Zircaloy-2 substrate surface were determined. Since active areas larger than the SECM probe tip were observed, and these active areas were embedded in surroundings with low surface reactivity, the probe size is not an issue; the sizes of the probe tip and active areas were input to the COMSOL model, and the active areas assumed to be isolated from each other. The analytical solutions of Lefrou and Cornut,[36] which link the rates of surface reactions to the
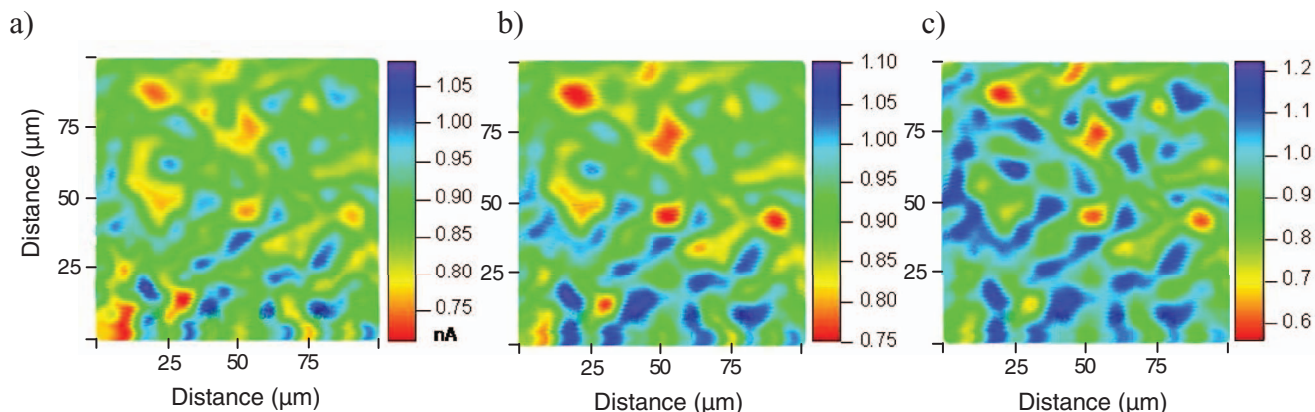
Figure 3. SECM images recorded on a Zircaloy-2 sample at applied substrate potentials of (a) -1.3 V_{SCE}, (b) -1.6 V_{SCE}, and (c) -1.9 V_{SCE}. The relationship between current and color for each panel is given by the color bar, scaled in nA, to the right of each SECM image.
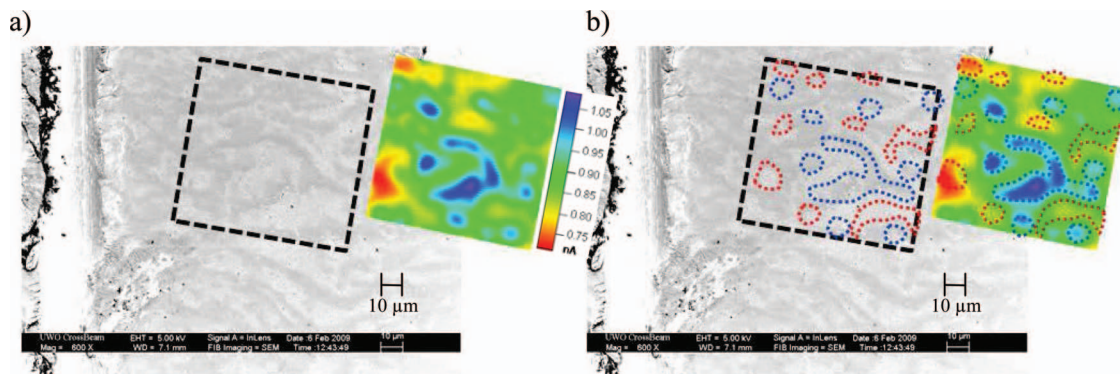
Figure 4. Superposition of SEM and SECM images: (a) Original SEM and SECM images of the same region on a Zircaloy-2 surface; (b) α- (light) and β-phase regions in the SEM image superimposed with low (red) and high (blue) current areas in the SECM image, respectively. SECM imaging was carried out in a 0.9 mM ferrocenemethanol + 0.1 M Na_2SO_4 solution using a 7 μm carbon UME with a RG value of 3. Potentials of 0.23 V_{SCE} and −1.32 V_{SCE} were applied to the UME tip and sample, respectively. The overlapping SECM images have a normalized current scale that ranges from 0.63 to 0.96 nA.
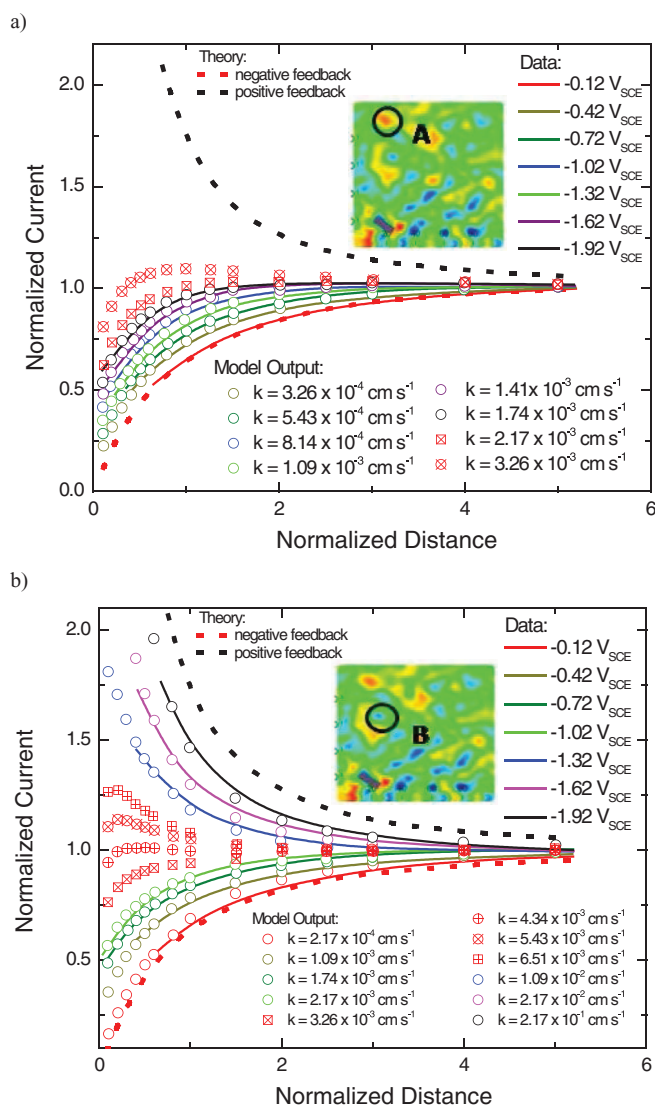
Figure 5. Normalized probe approach curves (solid curves) recorded at various substrate potentials (i.e., experimental data), taken at (a) location A (low current region) on the inset SECM image, and (b) location B (high current region) on the inset SECM image, superimposed on simulated PACs (symbols) calculated for the given k values. For reference, the theoretical PACs for the full positive and negative feedback cases are also plotted (dashed curves).

currents measured during PACs, do not take into consideration the size of the active area on the substrate, and therefore were not used in our interpretations.

The form of the simulated approach curves can be changed all the way from full negative feedback to full positive feedback as the rate constant k is increased. Such a change indicates the ability of the substrate surface to regenerate the reduced form of the redox mediator (i.e., to reduce ferroceniummethanol to ferrocenemethanol) at a rate sufficient to keep up with the rate of its consumption at the probe tip. If regeneration is too slow, the probe approach curve will tend toward negative feedback, with full negative feedback observed when the rate of regeneration is zero; conversely, if redox mediator regeneration at the substrate is very fast, then approach curves will show positive feedback tendencies, with full positive feedback observed when the rate of redox mediator oxidation at the probe tip is limited only by diffusion of the mediator species from the substrate to the probe tip, and not by any mediator regeneration kinetics.

Figure 5a shows the experimental PACs taken at location A, with low activity, for different substrate potentials, compared to simulated PACs for different values of k. At the most noble substrate potential, −0.12 V_{SCE}, the α-phase region on the surface behaved like a pure insulator with a k value approaching zero. As the applied potential on the substrate was made more negative, the k value increased slightly with increased cathodic polarization, but feedback remained negative even at a potential as low as −1.92 V_{SCE}.

By contrast, PACs recorded on the grain boundary on location B, with high activity, in Figure 5b, show a switch from partial negative to partial positive feedback between −1.02 V_{SCE} and −1.32 V_{SCE}. This coincides with the region of the polarization curve within which the Tafel slope changes from −816 mV/decade to −243 mV/decade, Figure 2. However, even for the low potential range, −0.12 V_{SCE} to −0.9 V_{SCE}, the k values (Figure 6) determined from the PACs recorded at location B are higher than those for location A, suggesting that even when the whole surface appears passive, these latter locations are slightly more cathodically reactive than the surfaces of the α-grains, (Figure 5a).

Examples of EIS spectra recorded on Zircaloy-2 over the same applied potential range are shown in Figure 7. At small cathodic polarizations (−0.12 V_{SCE} to −0.92 V_{SCE}) the spectra exhibit two distinct features: a time constant at intermediate frequencies and a second response at low frequencies. As the polarization is made more cathodic, the phase angle related to the low frequency time constant (most clearly seen in Figure 7a) diminishes and the magnitude of the impedance (Figure 7b) decreases, consistent with the polarization behavior, which shows the magnitude of the steady-state cathodic current increasing over this potential range, Figure 2. The low frequency response disappears when the potential becomes more negative than −1.3 V_{SCE}; i.e., in the range where the Tafel slope
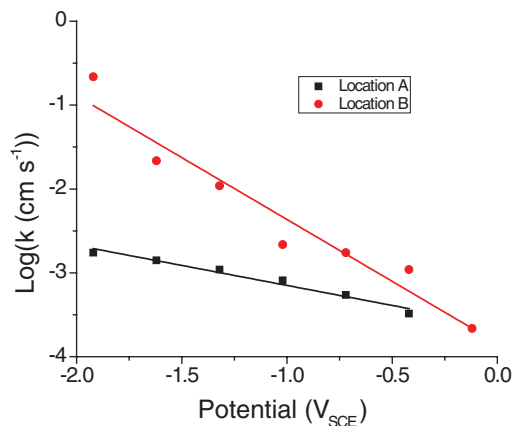
Figure 6. Rate constants (k), estimated by matching simulated PACs to experimental curves (Figure 5), plotted as a function of substrate potential.

increases, Figure 2, and the SECM begins to detect distinct reactive sites, Figure 3 and Figure 5b.

EIS spectra were fitted by one of two electrical equivalent circuits: one comprising a constant phase element (CPE) in parallel with a film resistance coupled to a Warburg impedance (W, representing a diffusion process within the film), all in series with the electrolyte resistance, circuit 1 in Figure 8a; or a similar circuit without the Warburg impedance, circuit 2 in Figure 8a. A CPE rather than a pure capacitance[37] was used to represent the potentially non-ideal film capacitance. The impedance response of the CPE, Z_{CPE}, is given by,

$$Z_{CPE} = Q^{-1}(j\omega)^{-\alpha} \qquad [4]$$

where Q is the CPE coefficient, α the exponent, and ω the angular frequency of the applied potential perturbation. Fitting generally yielded $\alpha \geq 0.9$, allowing the method of Brug et al.[37,38] to be used to convert
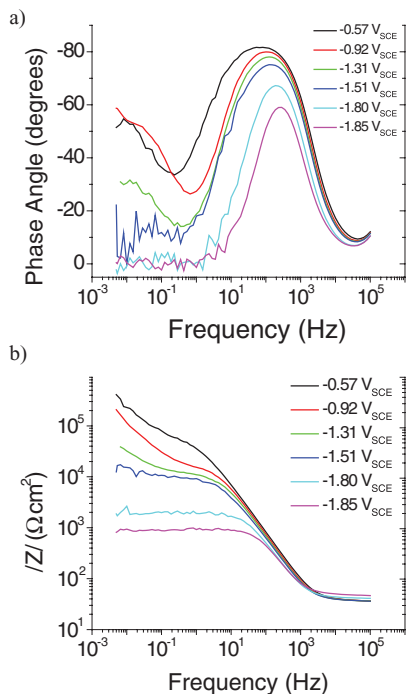
Figure 7. Bode plots for (a) the phase angle and (b) the magnitude of the impedance of a Zircaloy-2 sample, recorded in deaerated 0.1 M Na_2SO_4 at the applied potentials indicated.
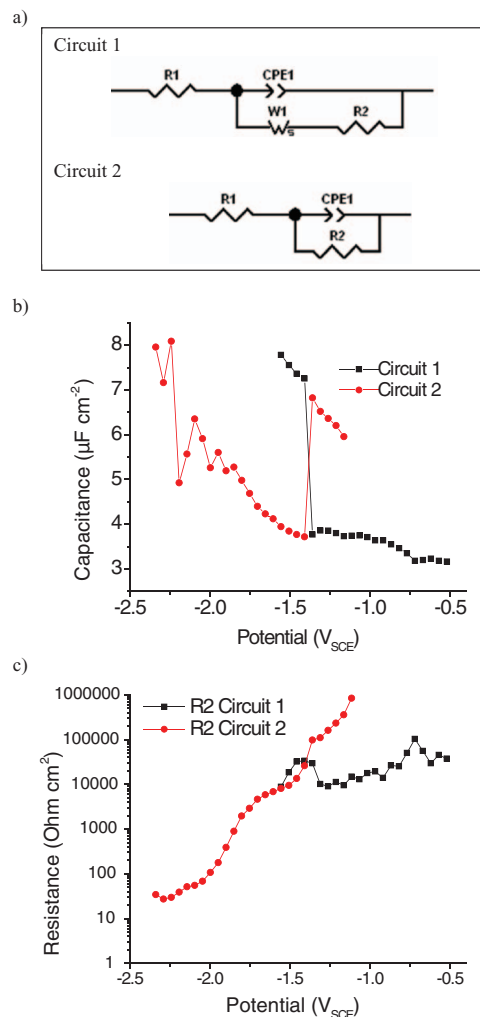

Figure 8. (a) Circuits 1 and 2 fitted to EIS data (Figure 7) to obtain (b) capacitance and (c) resistance values, at each applied potential.

the CPE parameter to an equivalent capacitance value:

$$C = \left[Q \left(\frac{1}{R_1} + \frac{1}{R_2} \right)^{(\alpha - 1)} \right]^{\frac{1}{\alpha}} \qquad [5]$$

The capacitance and resistance values determined by fitting one or other of these two circuits to the EIS spectra are shown in Figure 8b and 8c. For potentials > -1.3 V_{SCE}, the circuit including the Warburg element (circuit 1 in Figure 8a) was required to fit the data. The separate contributions to the impedance response are clearly visible in the phase angle plot, Figure 7a. Here the low impedance magnitude and phase angle at high frequencies represent the response of the electrolyte, R_1; the phase angle peak and rising impedance modulus at intermediate frequencies, the R_2C parallel combination; and the more slowly rising (with frequency) impedance modulus and increasing phase angle at low frequencies, the Warburg impedance, W.

At potentials < -1.3 V_{SCE}, at which hydrogen is produced, the Warburg element is no longer required. The need for two distinct circuits is very clear in Figure 8, and emphasized, especially in the capacitance plot, by the inclusion of several errant values obtained if the wrong circuit was used. The need for a Warburg element disappears at the potential at which the SECM detects a significant increase in reactivity in the grain boundary locations, but not on the grains, Figure 6, consistent with the SECM evidence that surface reactivity at boundaries dominates over that on grains.
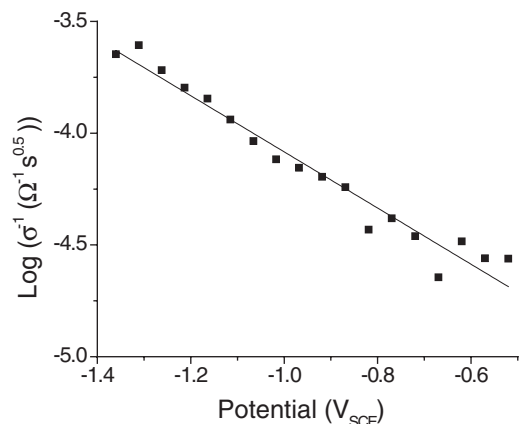
Figure 9. Values of the Warburg coefficient (σ) obtained by fitting circuit 1 (Figure 8a) to the measured EIS spectra.

For potentials >-1.3 V_{SCE}, the capacitance values are small and the resistance values large, consistent with the presence of a thin passive oxide. Using a dielectric constant of 28[39] and the equation for the capacitance of a parallel plate capacitor, an oxide film thickness of ∼7 nm is obtained, consistent with expectations for a thin passive film. This thickness (as indicated by the constant capacitance in Figure 8b) does not change significantly over the potential range -0.5 V_{SCE} to -1.3 V_{SCE}, indicating no decrease in film thickness with increasing cathodic polarization. Attempts to fit an equivalent circuit in which the Warburg element was replaced by a second parallel RC combination to represent discrete pores within the passive film to the spectra in this potential range were unsuccessful, indicating that the oxide contained a high density of fault sites, which would be seen in the impedance spectra as a general, rather than discrete, lowering of film resistance. The small currents, large resistances and Tafel slopes, need for a Warburg element, and the absence of differences in site reactivities in SECM maps suggest that the cathodic reaction, $2H_2O + 2e^- \rightarrow H_2 + 2OH^-$, occurs within a large number of fault locations within the passive oxide. The noise at the low frequency end of the EIS spectra would be expected for gas evolution within narrow faults. Since SECM shows grain boundary locations that eventually exhibit enhanced reactivity, it is likely that water reduction leading to H₂ production is occurring at oxide mismatches at these locations. Evaluation of the Warburg coefficient (σ) given by the relationship,

$$\sigma = \frac{RT}{\sqrt{2}n^2 F^2 C D^{1/2}} \qquad [6]$$

where R represents the universal gas constant, T the temperature, n the number of electrons being transferred, F Faraday's constant, C the concentration of diffusing species in the narrow fault sites, and D the diffusion coefficient, shows that the term CD increases with decreasing potential, Figure 9. Since the process leading to the changes in sigma involves a significant change in dimension of the fault sites, the effective diffusion coefficient almost certainly increases. However, this change will be convoluted with a change in pH (OH⁻ concentration) as H₂O reduction occurs more extensively, making a quantitative evaluation of the actual change in D impossible.

For potentials <-1.3 V_{SCE}, when the SECM analyses clearly indicate an enhanced reactivity in the grain boundaries, the need for a Warburg element disappears and the EIS spectra can be accurately fit with circuit 2 shown in Figure 8a. This opening of the grain boundaries between -1.0 V_{SCE} and -1.3 V_{SCE} is observed as an increase in the overall cathodic current, Figure 2, and in the value of the rate constant for the reduction of the redox mediator on the substrate, Figure 6.

The absence of a diffusion contribution to the impedance indicates that at that point H₂O has unlimited access to the alloy surface, and H₂ production at these locations leads to extensive noise in the low

frequency end of the EIS spectra, Figure 7, as well as in the cathodic currents recorded on the Zr (not shown). It is possible that this pore-opening process is enhanced by slight dissolution of the oxide film over secondary phases as the OH⁻ concentration at the alloy surface increases with increasing cathodic polarization, although such dissolution was not observed for an oxide film on pure Zr.[38]

The very large magnitude of the Tafel slope for E <-1.3 V_{SCE} indicates that water reduction is still highly polarized, despite the apparent open grain boundaries. A possible explanation for this is that, as the cathodic current increases, the SPPs and exposed β-phase at the grain boundaries are rapidly converted to a hydride,

$$Zr + xH_2O \rightarrow ZrH_x + xOH^- \qquad [7]$$
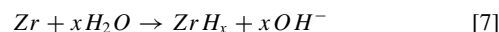
and this surface hydride layer polarizes the H₂O reduction reaction. Polarization of the water reduction reaction by formation of surface hydrides has been observed previously on Ti electrodes.[40] Second, the k value determined on grains (Figure 5a) remains potential-independent to potentials considerably more negative than the flat-band potential (-1.5 V_{SCE}), when the degeneracy would be expected, leading to oxide conductivity and an increase in H₂O reduction current. This indicates that once grain boundary locations are opened the interfacial potential drops across these locations, leaving the oxide unpolarized.

Conclusions

A combination of steady-state polarization curves, EIS, and SECM has been used to investigate the cathodic polarization of Zircaloy-2 in neutral 0.1 M sodium sulfate solution, with the primary goal of elucidating the possible pathways for hydrogen absorption into the alloy. Over the potential range from the open-circuit potential (~-0.1 V_{SCE}) to ~-1 V_{SCE} very low currents and a Tafel slope of 332 mV/decade indicated that water reduction was highly polarized on a passive oxide-covered surface. EIS spectra suggested that water reduction was occurring in fault sites in the oxide film, although SECM, using Fc as a redox mediator, did not detect any significant variations in reactivity across the alloy surface.

For potentials in the range -1 V_{SCE} to -1.3 V_{SCE}, significantly larger currents were observed, and SECM indicated the opening up of locally active sites on the Zircaloy-2 surface. By matching SECM images to SEM images it was demonstrated that these more reactive locations were associated with β-phase grain boundary sites between the α-grains of the alloy, with the most reactive sites likely to be the locations of secondary phase particles containing the impurities Fe, Ni, and Cr as Zr(Fe, Cr)₂ and Zr₂(Fe, Ni). The need for a Warburg element in fitting EIS spectra indicates that H₂O reduction is confined to tight flaws in the oxide or reduced oxide at these locations.

Further cathodic polarization to potentials ≤-1.3 V_{SCE} showed that the current for water reduction steadily increased with increasing polarization, although the observed Tafel slope of -243 mV/decade suggested the reaction might be strongly polarized on a surface hydride layer. The lack of a diffusion contribution to EIS spectra in this potential range is consistent with the increased size of these locations as indicated by SECM.

Probe approach curves were used to determine the differences in the rate constant for reduction of the mediator on α-grains and within β-phase grain boundaries. These rate constants confirmed the steady increase in reactivity in the grain boundaries, compared to only a very small increase in reactivity on the grains. We conclude that once the grain boundaries were activated, the interfacial potential dropped across these locations leaving the oxide unpolarized. These results indicate that grain boundaries, and especially sites decorated with secondary phase particles, could be the primary routes for hydrogen absorption into the alloy. Mapping hydrogen concentration profiles above the Zr sample is in progress, using the substrate generation and tip collection mode. This should provide direct evidence of the extent of hydrogen evolution occurring in the vicinity of such flaws.

References

1. C. C. Moya, M. J. Iribarren, N. Di Lalla, and F. Dyment, *J. Nucl. Mater.*, **382**, 35 (2008).
2. M. J. Iribarren, M. M. Iglesias, and F. Dyment, *Metall. Mater. Trans. A-Phys. Metall. Mater. Sci.*, **33**, 797 (2002).
3. N. Nieva and D. Arias, *J. Nucl. Mater.*, **359**, 29 (2006).
4. P. Rudling and G. Wikmark, *J. Nucl. Mater.*, **265**, 44 (1999).
5. A. R. Massih, T. Andersson, P. Witt, M. Dahlback, and M. Limback, *J. Nucl. Mater.*, **322**, 138 (2003).
6. Y. Hatano, K. Isobe, R. Hitaka, and M. Sugisaki, *J. Nucl. Sci. Technol.*, **33**, 944 (1996).
7. B. Cox and H. I. Sheikh, *J. Nucl. Mater.*, **249**, 17 (1997).
8. J. A. Sawicki, *J. Nucl. Mater.*, **228**, 238 (1996).
9. X. Y. Meng and D. O. Northwood, *J. Nucl. Mater.*, **168**, 125 (1989).
10. C. Degueldre, J. Raabe, G. Kuri, and S. Abolhassani, *Talanta*, **75**, 402 (2008).
11. R. K. Zhu, C. Nowierski, Z. F. Ding, J. J. Noël, and D. W. Shoesmith, *Chem. Mater.*, **19**, 2533 (2007).
12. R. K. Zhu, Z. Q. Qin, J. J. Noël, D. W. Shoesmith, and Z. F. Ding, *Anal. Chem.*, **80**, 1437 (2008).
13. C. Nowierski, J. J. Noël, D. W. Shoesmith, and Z. F. Ding, *Electrochem. Comm.*, **11**, 1234 (2009).
14. B. Cox, *Zirconium Intermetallics and Hydrogen Uptake During Corrosion*, Atomic Energy of Canada Ltd., Report AECL-9383, 1987.
15. Y. Hatano, R. Hitaka, M. Sugisaki, and M. Hayashi, *J. Nucl. Mater.*, **248**, 311 (1997).
16. R. M. Torresi, O. R. Camara, C. P. Depauli, and M. C. Giordano, *Electrochim. Acta*, **32**, 1291 (1987).
17. Z. M. Jarzebski, *Oxide semiconductors*; Pergamon Press: New York, 1973; Vol. 4.
18. B. M. Ikeda and D. W. Shoesmith, *Industrial Experience with Titanium*, Atomic Energy of Canada Ltd., Report AECL-11750, COG-97-4-1, 1997.
19. T. Murai, M. Ishikawa, and C. Miura, *Boshoku Gijutsu*, **26**, 177 (1977).
20. Z. Tun, J. J. Noël, and D. W. Shoesmith, *J. Electrochem. Soc.*, **146**, 988 (1999).
21. T. Ohtsuka, M. Masuda, and N. Sato, *J. Electrochem. Soc.*, **134**, 2406 (1987).
22. P. Meisterjahn, H. W. Hoppe, and J. W. Schultze, *J. Electroanal. Chem.*, **217**, 159 (1987).
23. J. J. Noël, H. L. Jensen, Z. Tun, and D. W. Shoesmith, *Electrochem. Solid State Lett.*, **3**, 473 (2000).
24. G. Wittstock, M. Burchardt, S. E. Pust, Y. Shen, and C. Zhao, *Angew. Chem. Int. Ed.*, **46**, 1584 (2007).
25. S. Amemiya, A. J. Bard, F. R. F. Fan, M. V. Mirkin, and P. R. Unwin, In *Annu. Rev. Anal. Chem.*; E. S. Yeung and R. N. Zare, Eds., 2008; Vol. 1, p. 95.
26. A. J. Bard, In *Scanning Electrochemical Microscopy*; A. J. Bard and M. V. Mirkin, Eds.; Marcel Dekker, Inc.: New York, 2001, p. 1.
27. F. Hua, K. Mon, P. Pasupathi, G. Gordon, and D. W. Shoesmith, *Corrosion*, **61**, 987 (2005).
28. T. Murai, T. Isobe, and Y. Mae, *J. Nucl. Mater.*, **230**, 178 (1996).
29. B. Cox, *J. Nucl. Mater.*, **264**, 283 (1999).
30. B. Cox and Y. M. Wong, *J. Nucl. Mater.*, **270**, 134 (1999).
31. R. K. Zhu, S. M. Macfie, and Z. F. Ding, *J. Exp. Bot.* **56**, 2831 (2005).
32. R. K. Zhu and Z. F. Ding, *Can. J. Chem.*, **83**, 1779 (2005).
33. X. C. Zhao, M. N. Zhang, Y. T. Long, and Z. F. Ding, *Can. J. Chem.*, **88**(6), 569 (2010).
34. B. A. Boukamp, *J. Electrochem. Soc.*, **142**, 1885 (1995).
35. T. Murai, T. Isobe, and Y. Mae, *J. Nucl. Mater.*, **226**, 327 (1995).
36. C. Lefrou and R. Cornut, *Chem. Phys. Chem.*, **11**, 547 (2010).
37. G. J. Brug, A. L. G. Vandeneeden, M. Sluytersrehbach, and J. H. Sluyters, *J. Electroanal. Chem.*, **176**, 275 (1984).
38. J. J. Noël, D. W. Shoesmith, and Z. Tun, *J. Electrochem. Soc.*, **155**, C444 (2008).
39. T. Hurlen and S. Hornkjol, *Electrochim. Acta*, **32**, 811 (1987).
40. L. Yan, S. Ramamurthy, J. J. Noël, and D. W. Shoesmith, *Electrochim. Acta*, **52**(3), 1169 (2006).